



Impact of Wavefront Errors on Nulling Interferometric Performance and Mitigation Strategies by Spatial Filter

Semester Project

Author
Philipp A. Huber

Supervisor
Dr. Adrian Glauser

July 2021
Institute for Particle Physics and Astrophysics
Department of Physics
ETH Zurich

Abstract

Purpose: Nulling interferometers can be used to enhance the contrast between two close astronomical sources by blocking the light of on-axis objects and allowing the light of off-axis sources to pass. As such, they represent an ideal technology for the detection and characterization of exoplanets. A typical way to quantify the performance of a nulling interferometer is the so-called null depth. The null depth is, among other quantities, dependent on the root mean square (RMS) wavefront errors of the incoming wavefronts. To reduce wavefront errors and thus improve the null depth, a spatial filter in the form of a pinhole can be employed, which, however, comes at the cost of a reduced throughput through the system. As exoplanets already represent relatively faint sources, as much throughput as possible should be preserved, which leads to a trade-off between improving the null depth and decreasing the throughput. This work thus tries to estimate the maximally allowed RMS wavefront error, when a null depth of 10^{-6} and a throughput of 80% are required.

Methodology: As a first part of this work, a formalism is developed that can capture the relation between null depth, RMS wavefront error and pinhole diameter (throughput). In doing so, the so-called Zernike polynomials are used to model wavefront errors. The formalism is then used in two ways. First, it is used to study the impact of a variety of individual Zernike terms on null depth and throughput. Second, it is used to estimate the maximally allowed RMS wavefront error, as anticipated before. This wavefront error is made up of several Zernike terms and modeled using three different Zernike coefficient distributions, which correspond to a very simple, a more realistic and a third case that is supposed to emulate the effect of a deformable mirror.

Results: As for the individual Zernike terms, we mainly find that lower order terms have a larger negative impact on the null depth as compared to higher order terms. In regards to the wavefront errors and the three distributions, we find the maximally allowed RMS wavefront error to be approximately 0.002λ for the first (simple), 0.001λ for the second (more realistic) and 0.003λ for the third (deformable mirror) distribution.

Conclusion: The values for the allowed RMS wavefront errors are relatively small and it remains questionable, whether they can be achieved in reality or not. However, the main take away from the analysis performed in this work is that wavefront corrections, e. g. by employing a deformable mirror, are likely indispensable to reach the required null depth and throughput. In future work, it would be interesting to model more realistic wavefront errors and also compare the results found here to the case of using a single-mode fiber for filtering instead of a spatial filter. As such, the framework developed here could be used to define requirements for actual nulling interferometry missions dedicated to the detection of exoplanets.

Acknowledgements

First of all, I would like to thank Dr. Adrian Glauser and Prof. Dr. Sascha Quanz for giving me the chance to conduct a semester project in their group, when other interested people are numerous and available projects are scarce. Special thanks then again go to Dr. Adrian Glauser for his willingness to supervise my project, for his kind and expert support throughout it and for the many meetings and discussions we had during it.

Contents

| | | |
|----------|--|-----------|
| 1 | Introduction | 1 |
| 1.1 | Nulling Interferometry | 1 |
| 1.2 | Wavefront Errors | 3 |
| 1.3 | Spatial Filters | 4 |
| 1.4 | Project Objectives | 5 |
| 2 | Theory | 7 |
| 2.1 | Aberrated Wavefronts | 7 |
| 2.2 | Fraunhofer Diffraction of Aberrated Wavefronts | 9 |
| 2.3 | Spatial Filtering of Aberrated Wavefronts | 11 |
| 2.4 | Null Depth | 12 |
| 2.5 | Throughput | 13 |
| 2.6 | Nulling Interferometric Performance with Spatial Filtering | 13 |
| 3 | Methodology | 14 |
| 3.1 | Computations | 14 |
| 3.2 | Individual Zernike Terms | 14 |
| 3.3 | Zernike Distributions | 14 |
| 4 | Results | 16 |
| 4.1 | Impact of Individual Zernike Terms | 16 |
| 4.2 | Impact of Wavefront Errors | 18 |
| 5 | Discussion | 21 |
| 6 | Conclusion | 22 |
| | References | 24 |
| | Appendices | 25 |
| A | Impact of Wavefront Errors on PSF | 25 |

List of Figures

| | | |
|-----|---|----|
| 1.1 | Illustration of a two-telescope nulling interferometer. | 2 |
| 1.2 | Illustration of an ideal and an aberrated wavefront. | 3 |
| 1.3 | Comparison between an ideal wavefront and PSF and an aberrated wavefront and PSF. | 4 |
| 1.4 | Individual terms modeled by Zernike polynomials (e. g. astigmatism, pentafoil) are added up to form the total wavefront error (WFE). | 4 |
| 1.5 | Spatial Filter | 5 |
| 2.1 | Illustration of the setup with one aperture. | 9 |
| 2.2 | Illustration of the setup showing the input plane, first lens, initial PSF, filter (pinhole), filtered PSF, second lens and output plane. | 11 |
| 3.1 | Overview of the three coefficient distributions D1, D2 and D3 used in this work. | 15 |
| 4.1 | Null Depth and Throughput for individual Zernike terms for an RMS of 0.0001λ , 0.0005λ and 0.01λ | 17 |
| 4.2 | Null Depth and throughput for distributions D1 to D3. | 19 |
| 4.3 | Pinhole diameter and throughput versus RMS for given null depths, shown for distributions D1 to D3. | 20 |
| A.1 | Overview ($Z_1 - Z_4$) of wavefront errors (Zernike polynomials) and the impact they have on the PSF. | 25 |
| A.2 | Overview ($Z_5 - Z_{12}$) of wavefront errors (Zernike polynomials) and the impact they have on the PSF. | 26 |
| A.3 | Overview ($Z_{13} - Z_{20}$) of wavefront errors (Zernike polynomials) and the impact they have on the PSF. | 27 |
| A.4 | Overview (Z_{21}) of wavefront errors (Zernike polynomials) and the impact they have on the PSF. | 28 |

List of Tables

| | | |
|-----|--|---|
| 2.1 | Noll's indexing convention for the first thirty Zernike polynomials. | 8 |
|-----|--|---|

List of Abbreviations

| | |
|------|-------------------------------------|
| LIFE | Large Interferometer For Exoplanets |
| PSF | Point Spread Function |
| RMS | Root Mean Square |
| WFE | Wavefront Error |
| WF | Wavefront |

List of Symbols

| | |
|------------------------|---|
| A | Aperture function |
| A_0 | Approximately constant amplitude of a wavefront across an aperture |
| $A_{0,\text{ab}}$ | Approximately constant amplitude of an aberrated wavefront across an aperture |
| $A_{0,\text{id}}$ | Approximately constant amplitude of an ideal wavefront across an aperture |
| A_1 | Aperture function of the source aperture |
| A_2 | Aperture function of the pinhole |
| c | Speed of light |
| dS | Infinitesimal area element (Fraunhofer diffraction) |
| D | Aperture diameter |
| D_1 | Source aperture diameter |
| D_2 | Pinhole aperture diameter |
| δ_{m0} | Kronecker delta function |
| ΔW | Wavefront error |
| E | Amplitude of an electric field |
| E_0 | Initial amplitude of a spherical wavefront |
| $E_{\text{aberrated}}$ | Amplitude of aberrated electric field |
| E_{ideal} | Amplitude of ideal electric field |
| $E_{\text{spherical}}$ | Full, time-varying amplitude of a spherical wavefront |
| E_+ | Sum of ideal and aberrated amplitudes |
| E_- | Difference between ideal and aberrated amplitudes |
| $\mathcal{F}\{\cdot\}$ | Fourier transform |

LIST OF ABBREVIATIONS

| | |
|-----------------------------|--|
| $\mathcal{F}^{-1}\{\cdot\}$ | Inverse Fourier transform |
| i | Imaginary unit |
| I_{init} | Initial total intensity |
| I_{max}, I_{+} | Maximum intensity |
| I_{min}, I_{-} | Minimum intensity |
| j | Index of Zernike polynomials using Noll's convention |
| k_x | x -coordinate in frequency domain |
| k_y | y -coordinate in frequency domain |
| λ | Wavelength |
| m | Second index of Zernike polynomials using conventional notation |
| n | First index of Zernike polynomials using conventional notation |
| N | Null depth |
| N_n^m | Normalization constant for Zernike polynomials |
| P | Point in xy -plane (Fraunhofer diffraction) |
| π | Ratio of circle's circumference to its diameter |
| r | Radial coordinate/Distance of the area element dS to the point $P(x, y, z)$ (Fraunhofer diffraction) |
| r_{max} | Maximum value of radial coordinate |
| R | Distance of the aperture center to the point $P(x, y, z)$ (Fraunhofer diffraction) |
| R_n^m | Radial part of Zernike polynomials |
| ρ | Normalized, radial coordinate |
| σ | Root mean square of a wavefront error |
| t | Time coordinate |
| T | Throughput |
| θ | Angular coordinate |
| Θ | Heaviside step function |
| u | Cartesian coordinate |
| u_{max} | Maximum value of u -coordinate |
| v | Cartesian coordinate |

LIST OF ABBREVIATIONS

| | |
|------------|---|
| v_{\max} | Maximum value of v -coordinate |
| x | Cartesian coordinate |
| y | Cartesian coordinate |
| z | Cartesian coordinate |
| z_j | Zernike polynomial coefficient in Noll's notation |
| Z_j | Full Zernike polynomial in Noll's notation |
| Z_n^m | Full Zernike polynomial in conventional notation |

1 Introduction

This chapter is supposed to give an introduction to the concepts that are relevant for this project. It contains an introduction to nulling interferometry, wavefront errors and spatial filters and finally, an overview of the objectives of this work.

1.1 Nulling Interferometry

Principles of Nulling Interferometry

A nulling interferometer is an instrument that makes use of the interference properties of light. It can be used to image faint astronomical sources, which are in close proximity to a much brighter source, such as an exoplanet orbiting its star. A nulling interferometer can consist of two or more telescopes. An illustration of a two-telescope nulling interferometer is given in Figure 1.1. Shown in the top center of the figure is a star (red) and an orbiting exoplanet (blue), whose light beams enter the two telescope apertures and make their way through the instrument. The interferometer is positioned in a way such that the star light enters the telescopes “on-axis”, while the exoplanet light reaches the telescopes slightly “off-axis”. This has the consequence that the star light reaches the two telescopes at the same time, i. e. both beams are in phase, where the exoplanet light reaches the two apertures at slightly different times (due to a slight difference in the distance between the two apertures and the exoplanet) and both beams are thus out of phase.

As illustrated by the box labeled “ $+\pi$ ”, one of the two interferometer arms features a delay line that introduces a phase shift of half a wavelength in the incoming beams. After that, the beams of the two telescopes are combined in the beam combiner, which is illustrated in the lower of the two centered boxes. As shown, the two red beams arrive exactly out of phase in the beam combiner. This is the result of them arriving perfectly in phase at the two apertures, when only one of them has then been shifted by half a wavelength in the delay line. If now the distance between the two apertures is chosen just right, the two beams from the exoplanet will have arrived out of phase by exactly half a wavelength, such that in the beam combiner they are perfectly in phase again. As a result, the combination of the two exoplanet beams leads to constructive interference and in an amplification of the individual exoplanet signals, while the star light gets canceled out completely by destructive interference. This is illustrated in the upper of the two centered boxes.

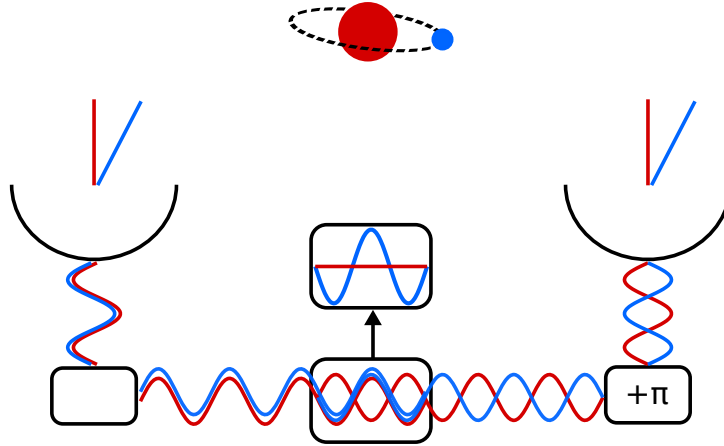


Figure 1.1: Illustration of a two-telescope nulling interferometer observing a star (red) and an orbiting exoplanet (blue). The signals of the two sources are combined in such a way that ideally the star signal is canceled out completely by destructive interference, while the exoplanet signal is amplified by constructive interference. Illustration inspired by ESA/Medialab (2002).

Assessing Nulling Interferometric Performance

In reality, the beams in the beam combiner will be subject to wavefront errors (more on wavefront errors in Section 1.2), resulting in limitations in terms of how well the two signals can be suppressed or amplified, respectively. This will in turn lead to limitations of the contrast that can be achieved between the two objects. A simple way to quantify how well the “nulling” works is the so-called “null depth”. The null depth is defined as the ratio between the minimum and the maximum intensity that can be produced in the interferometer, i. e.

$$N = \frac{I_{\min}}{I_{\max}}. \quad (1.1)$$

To get an intuitive idea of this quantity, it can be imagined as more or less corresponding to the ratio of the red signal and the blue signal, as they are produced in the beam combiner in Figure 1.1. With this picture in mind, it is straightforward to see that the ideal value for the null depth is zero and in general, the smaller the null depth, the better it is. A typical value for real applications could be 10^{-6} , for instance.

LIFE - Large Interferometer For Exoplanets

An example of a space-based four-telescope nulling interferometer is the so-called Large Interferometer For Exoplanets (LIFE). (Quanz et al., 2021) LIFE was initiated in 2017 and aims to develop the science, technology and roadmap for a space mission that will enable us to detect hundreds of nearby exoplanets, among them dozens similar to Earth, and analyze their atmospheres (LIFE Project, n. d.). According to LIFE Project (n.

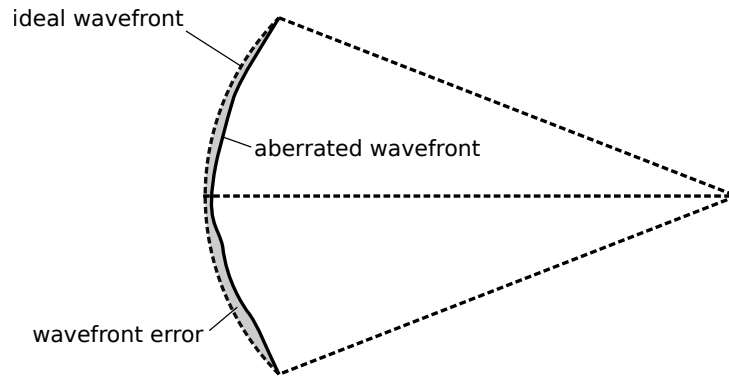


Figure 1.2: Illustration of a cross section of an ideal spherical wavefront (dotted curve), an aberrated wavefront (solid curve) and the corresponding wavefront error (gray area). Illustration inspired by Voelz (2011).

d.), the mission will be searching for habitable conditions and indications of biological activity and thus help us understand our place in the cosmic neighborhood.

1.2 Wavefront Errors

What Are Wavefront Errors?

Wavefront errors describe the difference between an actual, aberrated wavefront and an ideally shaped one. For the case of a spherical wavefront, for instance, Figure 1.2 illustrates the wavefront error as a gray area, corresponding to the difference between the ideal wavefront and the aberrated wavefront. Wavefront errors can be divided into two groups: intrinsic errors and induced errors. Intrinsic ones can be caused conical surfaces, glass media and fabrication errors, while induced ones have external causes, such as alignment errors, surface deformations by thermal variations, gravity and improper mounting and air turbulence in the atmosphere (telescope-optics.net, n. d.).

As mentioned in Section 1.1, wavefront errors can have a negative impact on nulling interferometric performance, particularly on the null depth. Obviously, the larger the wavefront error, the worse the null depth is going to be. In the following, the “magnitude” of a total wavefront error will be quantified by its root mean square (RMS). Details about the definition of the RMS wavefront error are given in Section 2.1. To get an idea how a wavefront error can impact performance, consider the illustrations in Figure 1.3. The first image on the left shows a circular aperture that acts as the source of an ideal wavefront, as seen head-on. Apparently, the wavefront simply corresponds to a perfectly flat surface. The second image from the left shows the resulting ideal point spread function (PSF). Note the perfectly rotational symmetric shape of the central lobe and the first ring of the Airy disk. The second image from the right shows an aberrated wavefront. It looks comparatively complex and no longer like a flat surface. The resulting aberrated PSF is illustrated on the right of it. Note that now neither the central lobe nor the first ring of the Airy disk are rotational symmetric and both look more complex as well.

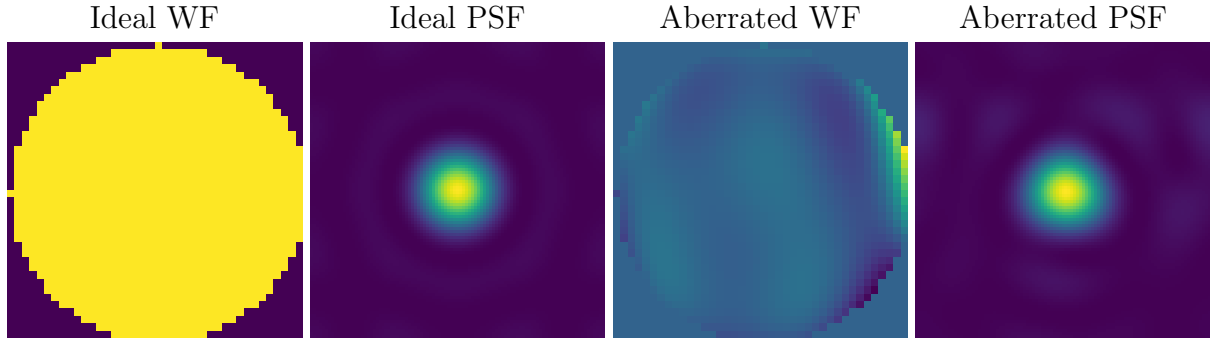


Figure 1.3: Comparison between an idela wavefront (WF)/PSF (first from left) and the resulting ideal PSF (second from left) and an aberrated WF (second from right) and the resulting aberrated PSF (first from right).

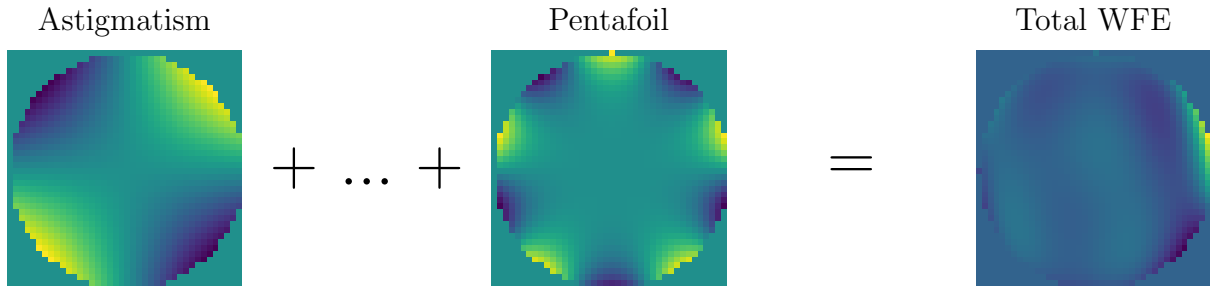


Figure 1.4: Individual terms modeled by Zernike polynomials (e. g. astigmatism, pentafoil) are added up to form the total wavefront error (WFE).

Modeling Wavefront Errors

A natural question is now how these complexly shaped wavefront errors can be modeled mathematically. A particularly nice way to do this is by employing the so-called Zernike polynomials. The Zernike polynomials are a complete set of orthogonal (in a continuous fashion) functions that are defined on the unit circle. The precise mathematical definition is given in Section 2.1. A complex wavefront error can then be modeled by decomposing it into individual terms that each contribute more or less strongly to it, while the individual terms can be modeled using the Zernike polynomials. Consider, for instance, Figure 1.4. The total wavefront error on the right can be modeled as a sum of individual wavefront error terms, such as astigmatism, pentafoil and so on. An overview of the first twenty-one Zernike terms and the corresponding PSFs is given in appendix A.

1.3 Spatial Filters

Spatial filters can be used to block certain spatial frequencies (Wallner et al., 2003). A spatial filter can be realized very easily by a pinhole, which is also the configuration that was used in this work. Figure 1.5 illustrates the use of a spatial filter for filtering an ideal PSF. As shown, the pinhole diameter is chosen in a way such that only the central

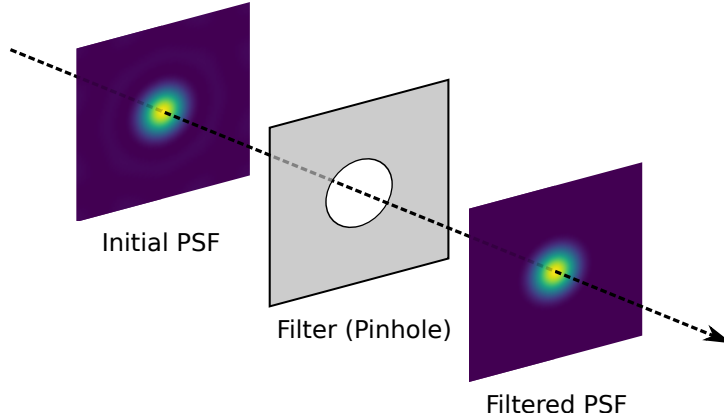


Figure 1.5: Spatial Filter

lobe of the initial PSF makes it through the filter. As a result, the first ring of the Airy disk that is slightly visible in the initial PSF, is no longer present in the filtered PSF. Of course, this pinhole diameter can be varied. Consider, for instance, that both of the interferometer arms, as depicted in Figure 1.1, features such a spatial filter. If we then decrease the pinhole diameter towards zero, the resulting null depth would tend towards zero as well, i. e. would tend towards the ideal value. However, at the same time, also the throughput we get would tend towards zero. This is of course not desirable, as, in the case of exoplanets, we are already dealing with faint sources and want to preserve as much light as possible. Hence, there is a trade-off between improving the null depth and decreasing the throughput.

1.4 Project Objectives

In Sections 1.2 and 1.3, we have seen that the null depth is dependent on the RMS wavefront error and the pinhole diameter. In addition, these two quantities, especially the pinhole diameter, also influence the throughput. For the reliable detection of small exoplanets, as it is planned by the LIFE mission, a null depth of 10^{-6} is required. At the same time, the throughput should not go below a value of 80%. A natural question, which is also the main question that should be addressed in this work, is then:

“What is the maximally allowed RMS wavefront error, if a null depth of $N = 10^{-6}$ and a throughput of $T = 80\%$ should be achieved?”

In addition, it would be interesting to understand the impact of a deformable mirror on this value. A deformable mirror may be used to correct some of the wavefront errors before they pass the spatial filter. Note that for simplicity, in the following we assume a two-telescope nulling interferometer, where one of the interferometer arms receives aberrated wavefronts, while the other one receives only ideal wavefronts.

The thesis is structured in the following manner. In Chapter 2, the theoretical framework that has been developed as a part of this project is presented. In Chapter 3, the

1.4. PROJECT OBJECTIVES

methodologies are explained and in Chapter 4, the results are presented. Chapter 5 features a discussion of the results and finally, Chapter 6 contains the conclusion to this project.

2 Theory

This chapter contains the theoretical framework that was used and/or developed as a part of this project. It features an explanation of how wavefront errors and aberrated wavefronts can be modeled, how these aberrated wavefronts behave in the context of Fraunhofer diffraction and, most importantly, how they behave in a spatial filter setup. Moreover, it gives a precise definition of the null depth and throughput in the context of spatial filtering with a two-telescope nulling interferometer. Finally, the null depth is expressed in a manner that captures its relation to the RMS wavefront error and the pinhole diameter and thus combines the essence of the main question of this work in one equation.

2.1 Aberrated Wavefronts

Zernike Polynomials

As anticipated in Section 1.2, wavefront errors can be modeled using Zernike polynomials. Any specific Zernike polynomial is specified by two indices $n, m \in \mathbb{N}_0$ with $n \geq m$. They can be expressed as

$$Z_n^m(\rho, \theta) = N_n^m R_n^{|m|}(\rho) \cdot \begin{cases} \cos m\theta, & m \geq 0 \\ (-\sin |m|\theta), & m < 0, \end{cases} \quad (2.1)$$

where δ_{m0} is the Kronecker delta function. The normalization N_n^m is given by

$$N_n^m = \sqrt{\frac{2(n+1)}{1 + \delta_{m0}}} \quad (2.2)$$

and the radial part $R_n^m(\rho)$ by

$$R_n^m(\rho) = \begin{cases} \sum_{k=0}^{\frac{n-m}{2}} \frac{(-1)^k (n-k)!}{k! \left(\frac{n+m}{2} - k\right)! \left(\frac{n-m}{2} - k\right)!} \rho^{n-2k}, & n - m \text{ even} \\ 0, & n - m \text{ odd} \\ 1, & \rho = 1 \end{cases} \quad (2.3)$$

with $\rho = r/r_{\max}$ the normalized radial coordinate. The normalization of the radial coordinate results in the units of the Zernike polynomials to be unity. For simplification,

2.1. ABERRATED WAVEFRONTS

| n, m | j | n, m | j | n, m | j | n, m | j | n, m | j | n, m | j |
|--------|-----|--------|-----|--------|-----|--------|-----|--------|-----|--------|-----|
| 0, 0 | 1 | 2, 2 | 6 | 4, 0 | 11 | 5, 1 | 16 | 5, -5 | 21 | 6, 4 | 26 |
| 1, 1 | 2 | 3, -1 | 7 | 4, 2 | 12 | 5, -1 | 17 | 6, 0 | 22 | 6, -6 | 27 |
| 1, -1 | 3 | 3, 1 | 8 | 4, -2 | 13 | 5, 3 | 18 | 6, -2 | 23 | 6, 6 | 28 |
| 2, 0 | 4 | 3, -3 | 9 | 4, 4 | 14 | 5, -3 | 19 | 6, 2 | 24 | 7, -1 | 29 |
| 2, -2 | 5 | 3, 3 | 10 | 4, -4 | 15 | 5, 5 | 20 | 6, -4 | 25 | 7, 1 | 30 |

Table 2.1: Noll's indexing convention for the first thirty Zernike polynomials.

we can introduce Noll's indexing convention to write the Zernike polynomials Z_n^m with just one instead of two indices as Z_j . The conversion is given by

$$j = \frac{n(n+1)}{2} + |m| + \begin{cases} 0, & m > 0 \wedge (n \bmod 4) \in \{0, 1\} \\ 0, & m < 0 \wedge (n \bmod 4) \in \{2, 3\} \\ 1, & m \geq 0 \wedge (n \bmod 4) \in \{2, 3\} \\ 1, & m \leq 0 \wedge (n \bmod 4) \in \{0, 1\}. \end{cases} \quad (2.4)$$

The conversions for the first thirty Zernike polynomials are listed in Table 2.1.

Wavefront Errors

Wavefront errors can then be modeled as a sum of multiple Zernike polynomials, each preceded by a coefficient z_j specifying the contribution of the term, i. e.

$$\Delta W(\rho, \theta) = \sum_j z_j Z_j(\rho, \theta). \quad (2.5)$$

Note that the coefficients and, as such, also $\Delta W(\rho, \theta)$ have of units length. Equation (2.5) describes the deviation of the wavefront from a perfect wavefront. The RMS σ of the wavefront error can then be expressed as (Patil et al., 2014)

$$\sigma = \left[\overline{\Delta W^2} - (\overline{\Delta W})^2 \right]^{1/2} \quad (2.6)$$

$$= \left[\frac{1}{\pi} \int_0^{2\pi} \int_0^1 \Delta W^2(\rho, \theta) \rho d\rho d\theta - \frac{1}{\pi^2} \left(\int_0^{2\pi} \int_0^1 \Delta W(\rho, \theta) \rho d\rho d\theta \right)^2 \right]^{1/2} \quad (2.7)$$

$$= \left[\sum_j (z_j)^2 \right]^{1/2}, \quad (2.8)$$

where in (2.8) we have used the orthogonality relations of the Zernike polynomials. In the following, the wavefront errors and Zernike polynomials will be expressed in Cartesian

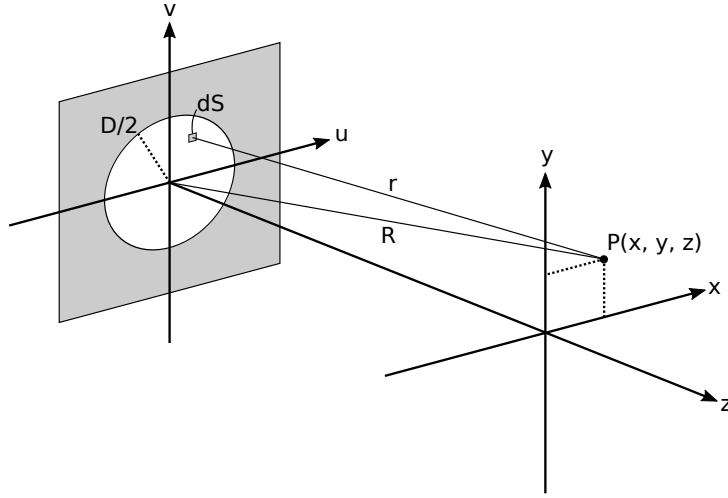


Figure 2.1: Illustration of the setup with one aperture.

coordinates u, v by introducing

$$\rho = \frac{\sqrt{v^2 + u^2}}{\sqrt{u_{\max}^2 + v_{\max}^2}}, \quad (2.9)$$

$$\theta = \arctan2(u, v). \quad (2.10)$$

Amplitude of an Aberrated Wavefront

The amplitude of a monochromatic, spherical wavefront at time t , at distance r from its source and subject to a wavefront error $\Delta W(u, v)$ is given by

$$E_{\text{spherical}}(t, r, u, v) = \frac{E_0}{r} e^{\frac{2\pi i}{\lambda}(ct - r - \Delta W(u, v))}, \quad (2.11)$$

where λ is the wavelength, c the speed of the wave and E_0 the initial amplitude. Note that an ideal wavefront can be modeled similarly simply by setting $\Delta W(u, v)$ to zero.

2.2 Fraunhofer Diffraction of Aberrated Wavefronts

The following will essentially be a derivation of Fraunhofer diffraction for the case of an aberrated wavefront. If planar waves hit an aperture, the aperture itself can be interpreted as the source of a wavefront with the amplitude given by (2.11). Consider the setup illustrated in Figure 2.1. To calculate the electric field at a point $P(x, y, z)$ after such an aperture, the following manipulations will become useful. The distance R from the center of the aperture to the point P can simply be written as

$$R = \sqrt{x^2 + y^2 + z^2}. \quad (2.12)$$

2.2. FRAUNHOFER DIFFRACTION OF ABERRATED WAVEFRONTS

For the distance of the infinitesimal surface element dS to point P we find

$$r = \sqrt{z^2 + (x - u)^2 + (y - v)^2} \quad (2.13)$$

$$= R \left(1 - \frac{2(ux + vy)}{R^2} \right)^{1/2} \quad (2.14)$$

$$\approx R \left(1 - \frac{ux + vy}{R^2} \right) \quad (2.15)$$

$$\approx R, \quad (2.16)$$

where in (2.14) we have used $R \gg D/2$, in (2.15) we have performed a Taylor series expansion and only kept the two first terms and in (2.16) we have assumed that $R \gg x, y$. The amplitude of the electric field at point $P(x, y, z)$ after the aperture, originating from the surface element dS within the aperture, can now be calculated as

$$dE(t, r, u, v) = E_{\text{spherical}}(t, r, u, v) du dv \quad (2.17)$$

$$\approx \frac{E_0}{R} e^{\frac{2\pi i}{\lambda} (ct - R + \frac{ux + vy}{R} - \Delta W(u, v))} du dv \quad (2.18)$$

$$\approx \underbrace{\frac{E_0}{R} e^{\frac{2\pi i}{\lambda} (ct - R)}}_{\approx \text{const.} \equiv A_0} e^{\frac{2\pi i}{\lambda} (\frac{ux + vy}{R} - \Delta W(u, v))} du dv, \quad (2.19)$$

where in (2.18) we have replaced the r in the denominator of $E(t, r, u, v)$ by (2.16) and the one in the exponential by (2.15) and in (2.19) we have simply rearranged the equation and defined A_0 . Note that $A_0 \approx \text{const.}$ if we assume that $R \approx \text{const.}$ and average over time t . Integrating now (2.19) over the aperture will yield the amplitude of the electric field. For convenience, we can introduce the aperture function

$$A(u, v) = \begin{cases} A_0, & \text{if } (u, v) \in \text{aperture} \\ 0, & \text{else} \end{cases} \quad (2.20)$$

with

$$A_0 \equiv \frac{E_0}{R} e^{\frac{2\pi i}{\lambda} (ct - R)} \approx \text{const.} \quad (2.21)$$

and then simply integrate from minus infinity to plus infinity. For a circular aperture of diameter D , for instance, the aperture function can be written as

$$A(u, v) = A_0 \Theta \left(\frac{D}{2} - \sqrt{u^2 + v^2} \right) \Theta \left(\sqrt{u^2 + v^2} \right), \quad (2.22)$$

where Θ is the Heaviside step function. The amplitude of the electric field at point P is thus given by

$$E(x, y) \approx \int_{-\infty}^{\infty} \int_{-\infty}^{\infty} A(u, v) e^{\frac{2\pi i}{\lambda} (\frac{ux + vy}{R} - \Delta W(u, v))} du dv. \quad (2.23)$$

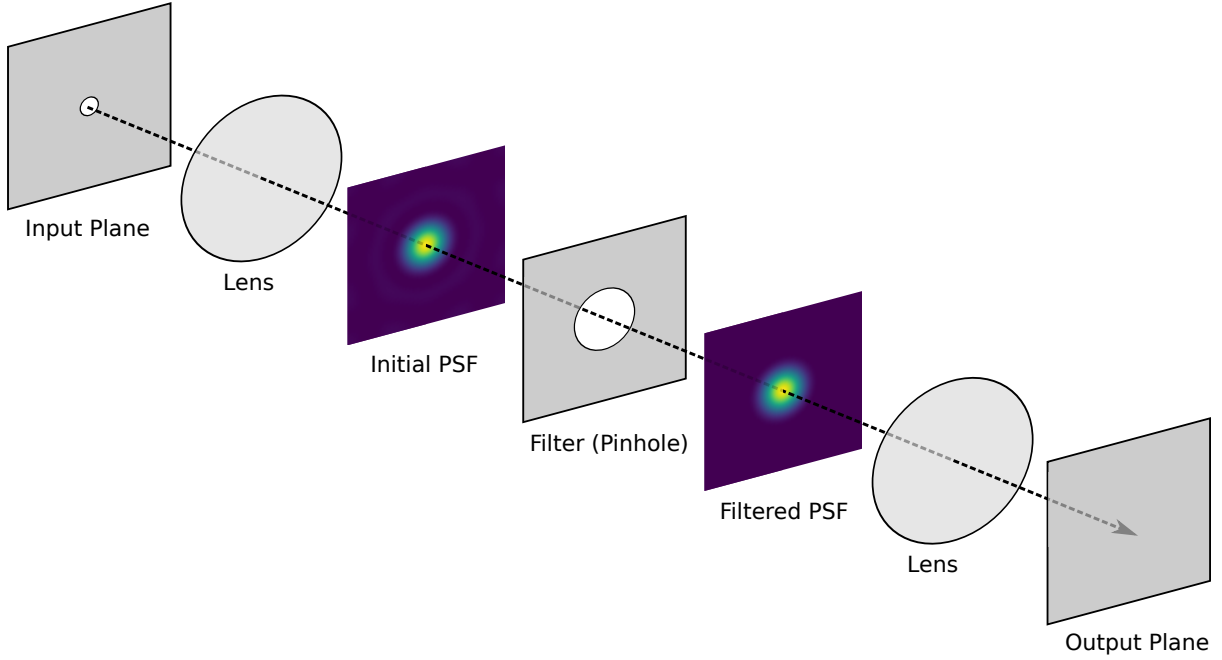


Figure 2.2: Illustration of the setup showing the input plane, first lens, initial PSF, filter (pinhole), filtered PSF, second lens and output plane.

Moving now to the frequency domain by introducing

$$k_x \equiv \frac{2\pi}{\lambda R}x, \quad (2.24)$$

$$k_y \equiv \frac{2\pi}{\lambda R}y \quad (2.25)$$

will simplify things a lot. Equation (2.23) will become

$$E(k_x, k_y) \approx \int_{-\infty}^{\infty} \int_{-\infty}^{\infty} A(u, v) e^{\frac{-2\pi i}{\lambda} \Delta W(u, v)} e^{i(k_x u + k_y v)} du dv \quad (2.26)$$

$$= \mathcal{F} \left\{ A(u, v) e^{-\frac{2\pi i}{\lambda} \Delta W(u, v)} \right\}. \quad (2.27)$$

Note that in the last step we have simply inserted the definition of the two-dimensional Fourier transform. The amplitude of the electric field at point P is thus given by the Fourier transform of the product of the aperture function and the exponential term corresponding to the aberrations. Omitting the aberrations, i. e. considering ideal wavefronts, would lead to the well-known Airy disk.

2.3 Spatial Filtering of Aberrated Wavefronts

To investigate the impact of a spatial filter on the electric field amplitude, consider the setup in Figure 2.2. The input plane is equivalent to the aperture plane in illustration 2.1

and contains the aperture with aperture function $A_1(u, v)$. Followed by the input plane is a lens that focuses the field on the filter plane, which is equivalent to the xy -plane in Figure 2.1 and contains the aperture function $A_2(k_x, k_y)$. After that we have a second lens that creates a collimated beam in the output plane with coordinates x, y . The final amplitude of the electric field in that plane is then given by the convolution of the first aperture function times the exponential term and the inverse Fourier transform of the second one, i. e.

$$E(x, y) = \left(A_1(u, v) e^{-\frac{2\pi i}{\lambda} \Delta W(u, v)} \right) * \mathcal{F}^{-1} \{ A_2(k_x, k_y) \} \quad (2.28)$$

$$= \mathcal{F}^{-1} \left\{ \mathcal{F} \left\{ A_1(u, v) e^{-\frac{2\pi i}{\lambda} \Delta W(u, v)} \right\} \cdot A_2(k_x, k_y) \right\}, \quad (2.29)$$

where in (2.29) we have used that the convolution of two functions is equal to the inverse Fourier transform of the product of the Fourier transforms of the two functions. Note that $A_2(k_x, k_y)$ is similarly defined to $A_1(u, v)$, but in the frequency domain. Also note that the coordinates u, v are identical to x, y , but used here to distinguish the different planes from each other.

2.4 Null Depth

In Section 1.1, we have introduced the null depth as the ratio between the minimum and the maximum intensity. We have also mentioned that these intensities correspond more or less to the red and blue signal in the beam combiner. In the following, we want to give a more precise definition of these definitions. As opposed to simply adding the two signals from both of the telescopes, we actually perform two distinct operations. That is, the two beams as given by equation (2.29) are constructively (+) and destructively (-) superimposed, which yields the total amplitudes

$$E_+(x, y) = E_{\text{ideal}}(x, y) + E_{\text{aberrated}}(x, y), \quad (2.30)$$

$$E_-(x, y) = E_{\text{ideal}}(x, y) - E_{\text{aberrated}}(x, y). \quad (2.31)$$

Remember that one interferometer arm is expected to only receive ideal wavefronts, while the other one receives aberrated ones. This results in the two intensities (neglecting some constants)

$$I_+(x, y) = |E_+(x, y)|^2, \quad (2.32)$$

$$I_-(x, y) = |E_-(x, y)|^2. \quad (2.33)$$

With this we can now define the null depth as

$$N(x, y) = \frac{I_-(x, y)}{I_+(x, y)}. \quad (2.34)$$

2.5 Throughput

Another quantity that was frequently mentioned in Chapter 1 was the throughput. To arrive at it, we first define the total initial intensity of the combined ideal and the aberrated wavefronts as

$$I_{\text{init}}(u, v) = \left| A_{0,\text{id}} + A_{0,\text{ab}} e^{-\frac{2\pi i}{\lambda} \Delta W(u,v)} \right|^2, \quad (2.35)$$

where $A_{0,i}$ is defined as in (2.21). In this particular work, the throughput is then defined as the ratio of the final intensity $I_+(x, y)$ of the combined wavefronts as given in (2.32) and $I_{\text{init}}(x, y)$, i. e.

$$T(x, y) = \frac{I_+(x, y)}{I_{\text{init}}(u, v)}. \quad (2.36)$$

2.6 Nulling Interferometric Performance with Spatial Filtering

For our setup in Figure 2.2, we can now express the relation between the null depth N and the pinhole diameter D_2 of the spatial filter and the RMS wavefront error σ as

$$N(x, y) = \left| \frac{\mathcal{F}^{-1} \left\{ A_2(k_x, k_y) \left(\mathcal{F} \left\{ A_1(u, v) \left(1 - e^{-\frac{2\pi i}{\lambda} \sum_j z_j Z_j(u,v)} \right) \right\} \right) \right\}}{\mathcal{F}^{-1} \left\{ A_2(k_x, k_y) \left(\mathcal{F} \left\{ A_1(u, v) \left(1 + e^{-\frac{2\pi i}{\lambda} \sum_j z_j Z_j(u,v)} \right) \right\} \right) \right\}} \right|^2 \quad (2.37)$$

where the RMS σ is implicitly contained in the Zernike coefficients z_j and with

$$A_1(u, v) = A_{10} \Theta \left(\frac{D_1}{2} - \sqrt{u^2 + v^2} \right) \Theta \left(\sqrt{u^2 + v^2} \right), \quad (2.38)$$

$$A_2(k_x, k_y) = \Theta \left(\frac{D_2}{2} - \sqrt{k_x^2 + k_y^2} \right) \Theta \left(\sqrt{k_x^2 + k_y^2} \right). \quad (2.39)$$

Note that we have arrived at equation (2.37) by inserting equations (2.29) - (2.33), (2.5) into equation (2.34) and using $a\mathcal{F}\{f(t)\} + b\mathcal{F}\{g(t)\} = \mathcal{F}\{af(t) + bg(t)\}$ or $a\mathcal{F}^{-1}\{f(t)\} + b\mathcal{F}^{-1}\{g(t)\} = \mathcal{F}^{-1}\{af(t) + bg(t)\}$, respectively.

3 Methodology

This chapter is used to present the methodologies that were employed in this work to arrive at the results.

3.1 Computations

The formalism introduced in Chapter 2 was meant to be used to address the main question of this work. For this reason, it was implemented into a Python-based software package, which could relatively quickly evaluate the relevant equations for different scenarios.

3.2 Individual Zernike Terms

To get an idea of the impact of the different wavefront error contributions, i. e. Zernike terms, a first analysis is focused on examining the null depth and throughput for individual Zernike polynomials, rather than total wavefront errors. In this work, the impact of the first twenty-one Zernike polynomials is investigated, all of which are assumed to have identical RMS values. The analysis is made for three different RMS values, namely 0.001λ , 0.005λ and 0.01λ .

3.3 Zernike Distributions

To address the main question of this project, the impact on null depth and throughput is then also investigated for wavefront errors. These wavefront errors are modeled as a sum of the first twenty-one Zernike terms. Judging by equation (2.5), we are left with the freedom to choose the individual Zernike coefficients. In this work, three different Zernike coefficient distributions were used, which are illustrated in Figure 3.1. The first distribution (D1) features equally distributed coefficients. This is probably the most simple case, however, it is not very realistic. A slightly more realistic approach is made by the second distribution (D2), which features unequally distributed coefficients that start large for low Zernike terms and decrease by a constant value for higher terms. Finally, the third distribution (D3) is almost identical to D2, however it lacks the first five Zernike terms. The impact of a wavefront error modeled with these three distributions is then investigated for different RMS values.

3.3. ZERNIKE DISTRIBUTIONS

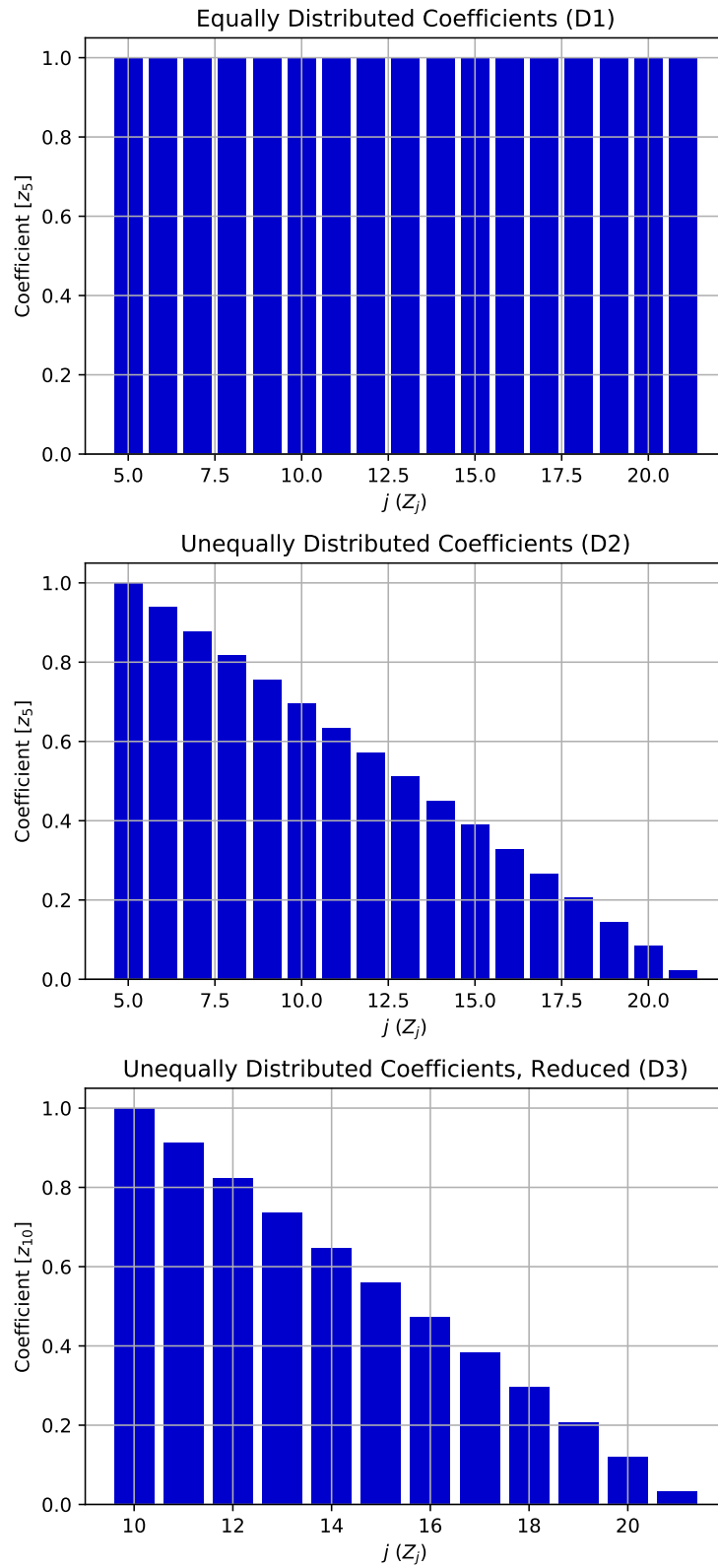


Figure 3.1: Overview of the three coefficient distributions D1, D2 and D3 used in this work.

4 Results

This chapter presents the results that have been produced during the project. It is divided in to two parts, one containing the results for the individual Zernike terms and one for the wavefront errors with distributions D1 to D3.

4.1 Impact of Individual Zernike Terms

Figure 4.1 shows the results for the individual Zernike terms. The left column shows the null depth for different RMS values, while the right column shows the corresponding throughput for the three cases. On the y -axes, we have the individual Zernike terms Z_1 to Z_{21} and on the x -axes, we have the pinhole diameter. Note that the white contour lines are identical for a given RMS and correspond to certain throughput values. We can now make several observations in these plots.

First of all, we can confirm that an increasing RMS leads to an increasing (worsening) null depth, as anticipated in Section 1.2. The throughput, however, remains mostly unaffected by the changing RMS values, at least for the parameter space we are considering here. Secondly, the influence of the pinhole diameter seems to be very significant on both the null depth and the throughput. Indeed, with very few exceptions, for a given Zernike term the data shows a better null depth for smaller pinhole diameters. This has already been mentioned in Section 1.2 as well. The throughput seems to be almost exclusively dependent on the pinhole diameter, independent of the specific Zernike term. The mapping of pinhole diameter to throughput, however, seems to be highly non-linear with relatively small increments in pinhole diameter for throughputs between 0% and 70% and increasingly large increments for higher throughputs. As a third point, we can now take a closer look at the differences between the different Zernike terms. All of the three null depth plots appear to have this yellowish, triangular feature. This tells us that, for a given pinhole diameter or throughput, respectively, higher Zernike terms can achieve a better null depth than lower terms. For our distributions D1 to D3, we can thus expect a more negative impact on the null depth by lower Zernike terms.

Finally, there are a few Zernike terms that seem to differ significantly from the others in terms of null depth for either very small or rather large pinhole diameters. For very small pinhole diameters, the Zernike terms Z_1 , Z_4 , Z_{11} and Z_{14} seem to correspond to much worse null depths than the other terms. In fact, they are the only terms that, for an increasing pinhole diameter, seem to increase in null depth before decreasing again.

4.1. IMPACT OF INDIVIDUAL ZERNIKE TERMS

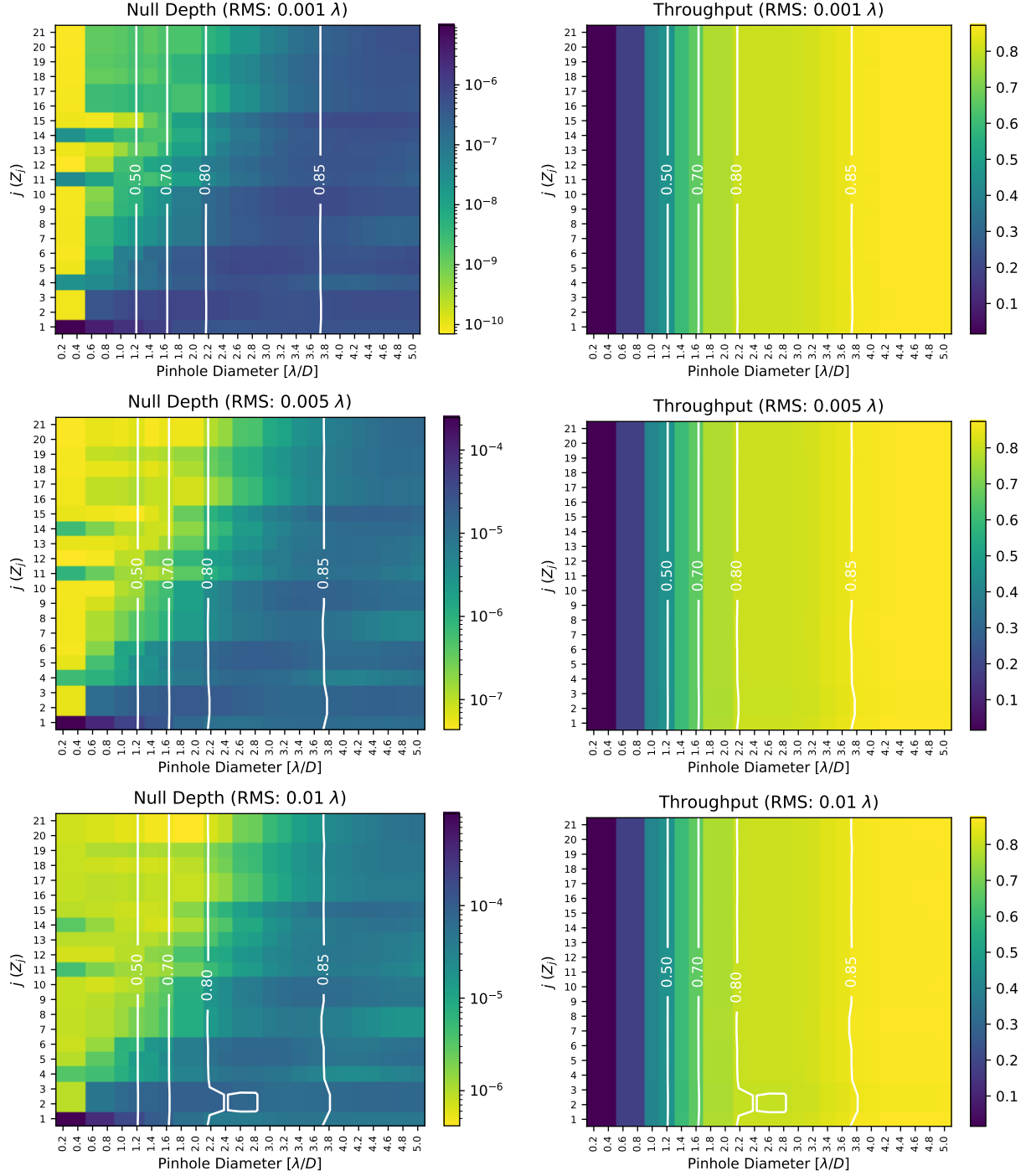


Figure 4.1: Null Depth and Throughput for individual Zernike terms for an RMS of 0.0001λ , 0.0005λ and 0.01λ .

A quick analysis, however, has shown that this is likely caused by numerical issues when performing the calculations and is not an actual physical effect. In fact, these issues occur for most Zernike terms for pinhole diameters of $0.2\lambda/D$ to $0.4\lambda/D$, so these value should not be given too much attention in any case. Also, for large pinhole diameters, the terms Z_2 , Z_3 , Z_5 , Z_6 , Z_9 , Z_{10} and Z_{15} seem to perform worse than the others. Having a look at the Zernike polynomials and the corresponding PSFs in Figures A.1 to A.4 in appendix A, we can identify possible reasons for these effects. Although the reason for the low values has been established to be of numerical nature, it is interesting to note that the four Zernike terms in question for the small pinhole diameters and their corresponding PSFs are all very close to being perfectly rotationally symmetric. For the larger pinhole diameters, however, the opposite seems to be the case. The Zernike terms themselves and their corresponding PSFs are significantly far away from being rotationally symmetric when compared to the other terms.

4.2 Impact of Wavefront Errors

In Figure 4.2, the null depth and throughput is illustrated for the three wavefront error distributions D1, D2 and D3. This time, the y -axis corresponds to the RMS values instead of the individual Zernike terms. Moreover, we now have a second contour line in black, which corresponds to certain null depth values. For the three plots showing the throughput, we can draw similar conclusions to the ones in Section 4.1, namely that, for the tested parameter space, it appears to be only dependent on the pinhole diameter. Also, the mapping from pinhole diameter to throughput shows the same non-linearities as before.

With the three plots showing the null depth we have now the ability to address the main question stated in Section 1.4, namely what is the maximally allowed RMS wavefront error if a null depth of 10^{-6} and a throughput of 80% should be achieved. For D1, we see that the two contour lines corresponding to these values cross at an RMS of approximately 0.002λ and a pinhole diameter slightly less than $1.8\lambda/D$. This RMS value decreases to around 0.001λ for the more realistic distribution D2. This is not unexpected, though, since we have anticipated in Section 4.1 that lower Zernike terms have a more negative impact on the null depth and they have higher coefficients than the higher terms in D2. Finally, if we move to D3, the RMS value increases to around 0.003λ . This, too, is expected, since some of the lower terms have been omitted in D3. Moreover, it suggests that employing a deformable mirror might indeed be useful to push the maximally allowed RMS value upwards. Finally, Figure 4.3 shows the isolated null depth contours from Figure 4.2 in a pinhole diameter/throughput versus RMS plot, assuming the throughput is constant for a given pinhole diameter.

4.2. IMPACT OF WAVEFRONT ERRORS

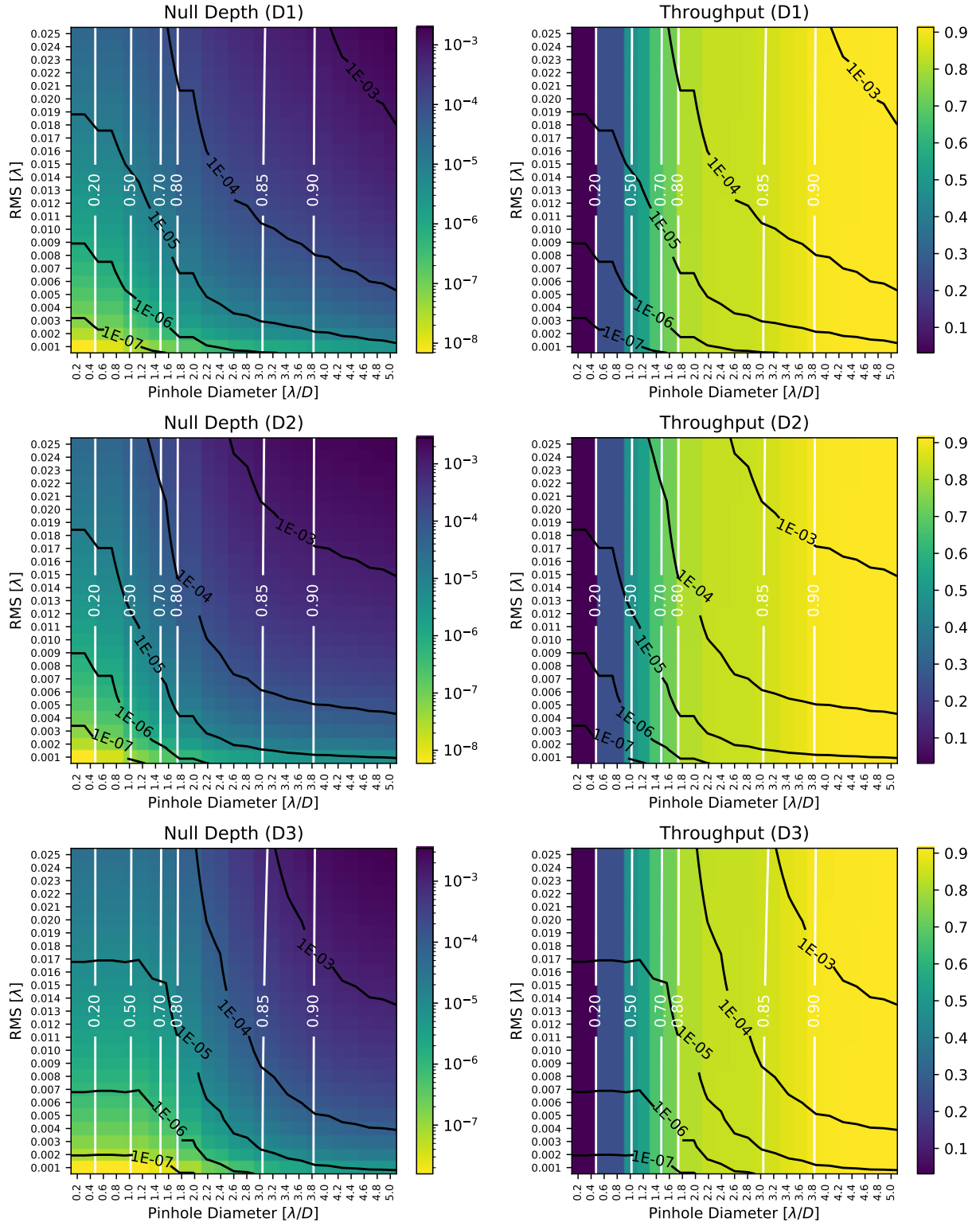


Figure 4.2: Null Depth and throughput for distributions D1 to D3.

4.2. IMPACT OF WAVEFRONT ERRORS

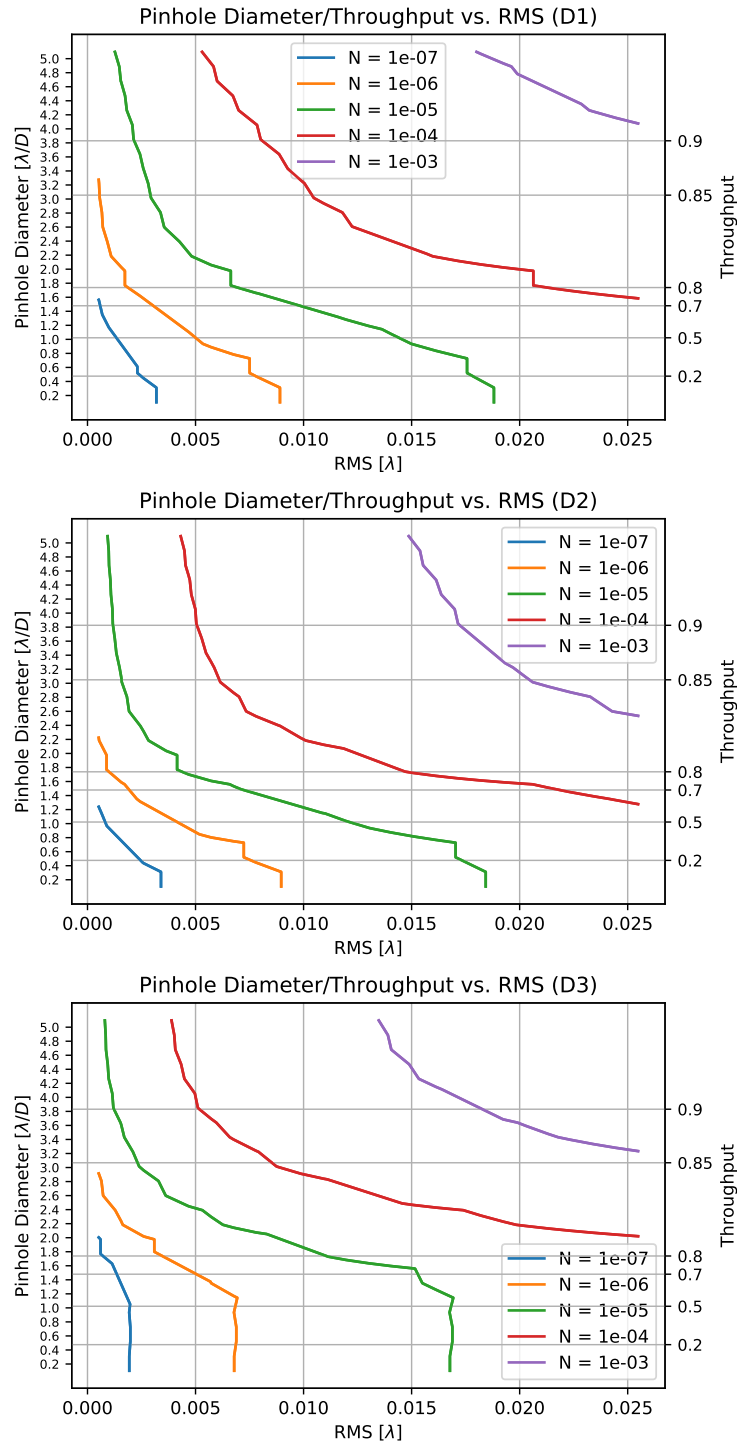


Figure 4.3: Pinhole diameter and throughput versus RMS for given null depths, shown for distributions D1 to D3.

5 Discussion

In this chapter, the results found in this work should be discussed.

Significance of the Results

In Section 4.2, we have presented the data that should help us address the main question of this project. We have identified the maximally allowed RMS value to be somewhere between 0.001λ and 0.003λ , depending on the distributions that is used to model the wavefront error. It should be mentioned at this point that these values ought to be used with caution due to the lack of uncertainty estimates on them. This is something that might be improved in the future. It can be said, however, that the values are relatively small, so the question remains how realistic it would be to actually reach them. It should be added that the values might become more realistic if more realistic distributions are used to model the wavefront error. Quite some time has been invested in looking for typical Zernike coefficient distributions for wavefront errors, however, nothing useful has been found. So for more solid results it might be necessary to revisit the task of finding such distributions. An other idea would be to employ Monte Carlo simulations to create the distributions in order to more thoroughly investigate the influence of the distribution on the results. Also, the impact of a deformable mirror on the Zernike coefficient distribution might be modeled in a more realistic way.

Possible Applications of the Framework

The theoretical framework and software that has been developed during this project may, in principle, be used to define instrumental requirements for an interferometry mission, such as the LIFE mission. In particular, knowing the maximally allowed RMS wavefront error, when a given null depth and throughput are to be reached, will give an understanding of the precision in the instrument optics that is needed to achieve these goals. It may then be estimated, what part of the RMS wavefront error may be corrected by correct alignment, mirror polishing, deformable mirrors, etc. To this end, it would also be interesting to extend the framework to the capability of modeling single-mode fibers. Single-mode fibers represent an alternative way of filtering a wavefront, for which it would be interesting to compare the results to the ones obtained in this work when using a spatial filter.

6 Conclusion

In this work, the relation between an RMS wavefront error, the pinhole diameter of a spatial filter and the null depth is investigated. More specifically, the maximally allowed RMS wavefront error that can be achieved by the use of a spatial filter, while requiring a null depth of 10^{-6} and a throughput of 80%, is identified. As a first part of the work, a formalism that can capture this relation is developed. Starting with aberrated wavefronts modeled using Zernike polynomials, the Fraunhofer diffraction of such wavefronts at a circular aperture is described, after which the impact of a pinhole in the focus plane is derived. Finally, the throughput and the null depth are defined.

The main question of this work is then addressed in two steps. As a first step, the impact of different Zernike terms should be understood, so the null depth and throughput are investigated for individual Zernike terms with varying RMS wavefront errors. The second then aims to get an estimate of the maximally allowed RMS wavefront error, so the null depth and throughput are investigated for a wavefront error modeled using Zernike terms up to the fifth order. More precisely, three different Zernike coefficient distributions are considered: an equal distribution, a linearly decreasing distribution containing higher values for lower order coefficients and a linearly decreasing distribution lacking certain lower order terms. The second distribution is meant to be slightly more realistic than the first one, while the third distribution roughly corresponds to what a deformable mirror might achieve.

As for the results, the analysis of the individual Zernike terms reveals mainly that lower order terms have a more negative impact on the null depth than higher order ones. Regarding the wavefront errors modeled with the three different distributions, the maximally allowed RMS wavefront errors is found to be approximately 0.002λ for the first, 0.001λ for the second and 0.003λ for the third distribution. Since these values are relatively small, it remains questionable whether they can actually be achieved in reality or not. However, the main take away from this analysis is that wavefront corrections, e. g. by employing a deformable mirror, are likely indispensable in order to reach the required null depth and throughput.

In terms of future work, it would be very interesting to repeat the calculations with more realistic wavefront errors or Zernike coefficient distributions in order to get a more realistic estimate of the maximally allowed RMS wavefront errors. Possibly, Monte Carlo simulations could be used in this matter. Moreover, it would be of great interest to see how the results obtained here would compare to the case of using a single-mode fiber instead of a spatial filter. In any case, this work has laid the foundations for a framework

that might potentially be used to define requirements for nulling interferometry space missions such as LIFE.

References

- ESA/Medialab. How nulling interferometry works, 2002. URL https://www.esa.int/ESA_Multimedia/Images/2002/03/How_nulling_interferometry_works. last accessed: July 12, 2021.
- LIFE Project. The large interferometer for exoplanets (life), n. d. URL <https://www.life-space-mission.com/>. last accessed: July 12, 2021.
- Abhijit Patil, Rajesh Langoju, and Pramod Rastogi. Signal-processing methods in phase-shifting interferometry. *Phase Estimation in Optical Interferometry*, XI:235–272, 2014. doi: 10.1201/b17701.
- S. P. Quanz, M. Ottiger, E. Fontanet, J. Kammerer, F. Menti, F. Dannert, A. Gheorghe, O. Absil, V. S. Airapetian, E. Alei, R. Allart, D. Angerhausen, S. Blumenthal, L. A. Buchhave, J. Cabrera, Ó. Carrión-González, G. Chauvin, W. C. Danchi, C. Dandumont, D. Defrère, C. Dorn, D. Ehrenreich, S. Ertel, M. Fridlund, A. García Muñoz, C. Gascón, J. H. Girard, A. Glauser, J. L. Grenfell, G. Guidi, J. Hagelberg, R. Helled, M. J. Ireland, R. K. Kopparapu, J. Korth, T. Kozakis, S. Kraus, A. Léger, L. Leedjårv, T. Lichtenberg, J. Lillo-Box, H. Linz, R. Liseau, J. Loicq, V. Mahendra, F. Malbet, J. Mathew, B. Mennesson, M. R. Meyer, L. Mishra, K. Molaverdikhani, L. Noack, A. V. Oza, E. Pallé, H. Parviainen, A. Quirrenbach, H. Rauer, I. Ribas, M. Rice, A. Romagnolo, S. Rugheimer, E. W. Schwieterman, E. Serabyn, S. Sharma, K. G. Stassun, J. Szulágyi, H. S. Wang, F. Wunderlich, M. C. Wyatt, and the LIFE collaboration. Large interferometer for exoplanets (life): I. improved exoplanet detection yield estimates for a large mid-infrared space-interferometer mission, 2021.
- telescope-optics.net. Telescope optical aberrations: Types and causes, n. d. URL <https://www.telescope-optics.net/aberrations.htm>. last accessed: July 13, 2021.
- David G. Voelz. Wavefront Aberrations. *Computational Fourier Optics: A MATLAB® Tutorial*, pages 141–168, 2011. doi: 10.1117/3.858456.ch8.
- Oswald Wallner, Walter R. Leeb, and Reinhold Flatscher. Design of spatial and modal filters for nulling interferometers. *Interferometry for Optical Astronomy II*, 4838:668, 2003. ISSN 0277786X. doi: 10.1117/12.456984.

Appendices

A Impact of Wavefront Errors on PSF

Figures A.1 to A.3 show an overview of the first 21 Zernike polynomials and their impact on a PSF.

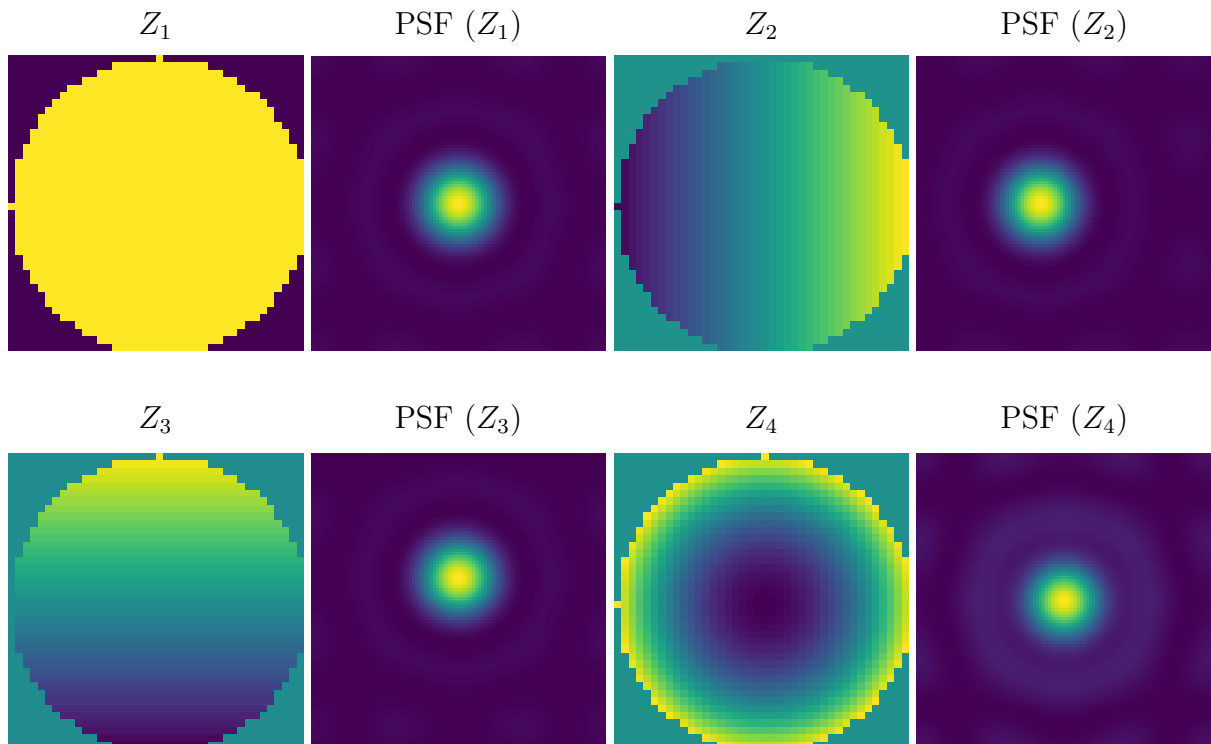


Figure A.1: Overview ($Z_1 - Z_4$) of wavefront errors (Zernike polynomials) and the impact they have on the PSF.

A. IMPACT OF WAVEFRONT ERRORS ON PSF

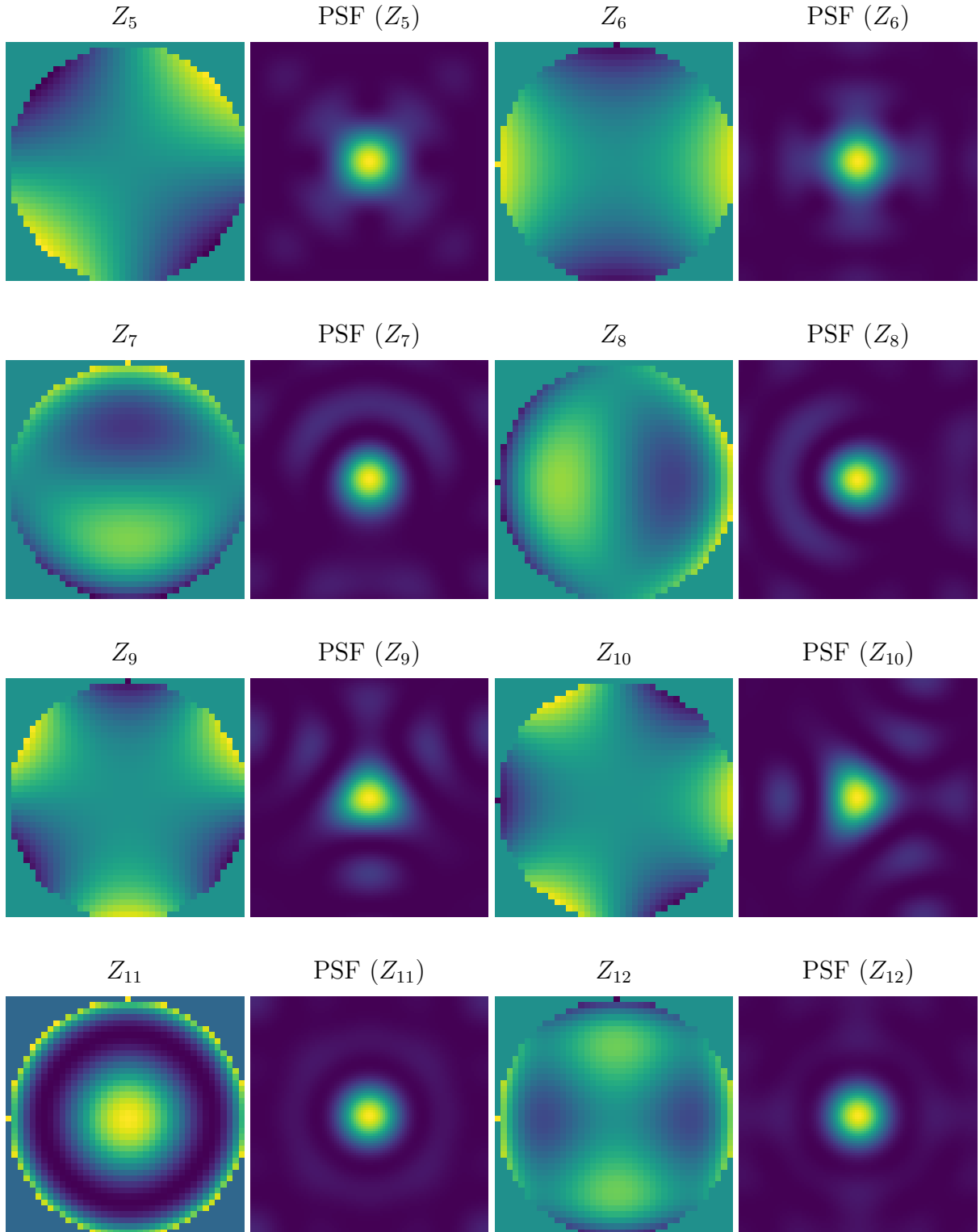


Figure A.2: Overview ($Z_5 - Z_{12}$) of wavefront errors (Zernike polynomials) and the impact they have on the PSF.

A. IMPACT OF WAVEFRONT ERRORS ON PSF

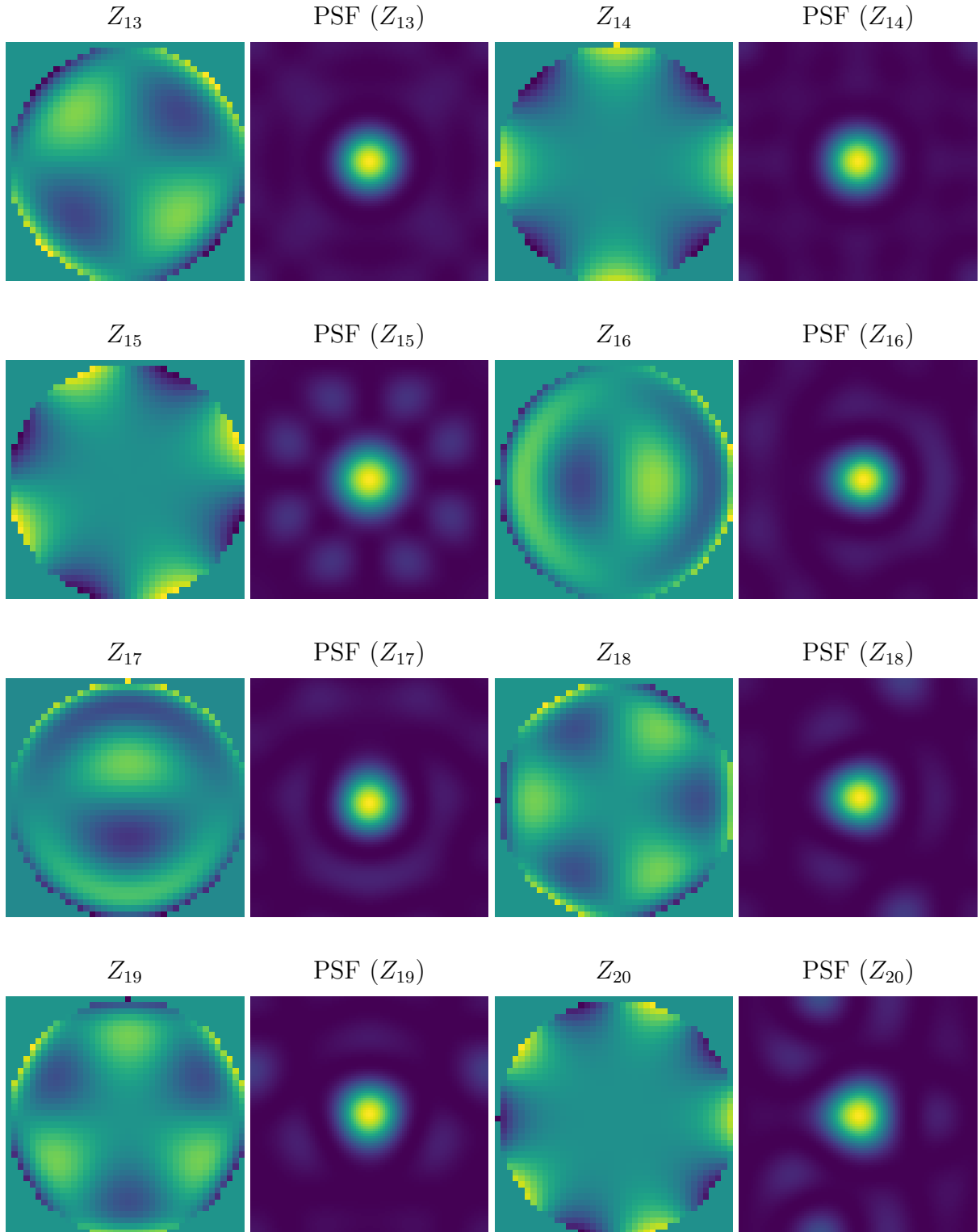


Figure A.3: Overview ($Z_{13} - Z_{20}$) of wavefront errors (Zernike polynomials) and the impact they have on the PSF.

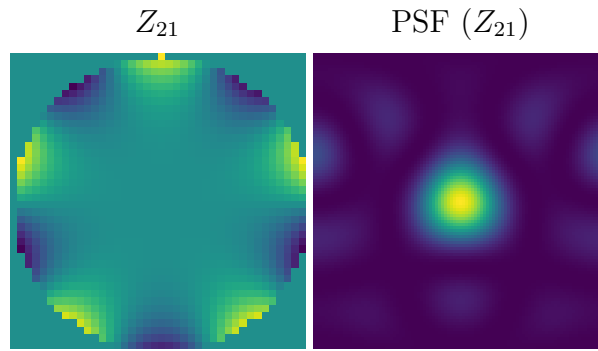


Figure A.4: Overview (Z_{21}) of wavefront errors (Zernike polynomials) and the impact they have on the PSF.